RSC Advances

PAPER

View Article Online
View Journal | View Issue

Cite this: *RSC Adv.*, 2017, **7**, 22599

The effect of rigid phenoxyl substituent on the NH_3-sensing properties of tetra-α-(4-*tert*-butylphenoxyl)-metallophthalocyanine/reduced graphene oxide hybrids†

Zheying Yu,[a] Bin Wang,*[a] Yong Li,[a] Di Kang,[a] Zhimin Chen[a] and Yiqun Wu*[ab]

Herein, we report a type of enhanced ammonia (NH_3) sensing materials formed by the functionalization of reduced graphene oxide (RGO) with 1,8,15,22-tetra-(4-*tert*-butylphenoxyl)-metallophthalocyanine (TBPOMPc, M = Cu, Ni, and Pb) *via* a solution self-assembly method based on π–π stacking interactions. The RGO/TBPOMPc hybrids exhibit excellent sensitivity, high response value, and fast response and recovery at room temperature, especially the RGO/TBPOPbPc sensor. The enhancement of the NH_3-sensing performance by TBPOMPc with a rigid phenoxyl-substituted group is attributed to the self-assembly behavior of TBPOMPc molecules. The rigid structure of TBPOMPc effectively prevents the intermolecular aggregation behavior. On the one hand, it expands the specific surface area of the RGO/TBPOMPc hybrids, which is propitious for the physical adsorption and diffusion of NH_3 molecules and reduces the response and recovery time. On the other hand, it weakens the electronic interaction between TBPOMPc molecules and results in reducing the resistance of charge transfer from NH_3 to TBPOMPc. Moreover, TBPOMPc is beneficial to enhance the sensitivity and selectivity of the RGO/TBPOMPc sensors towards NH_3. By contrast, the response of various RGO/TBPOMPc sensors decreases in the order of RGO/TBPOPbPc > RGO/TBPOCuPc > RGO/TBPONiPc. Furthermore, the rigid structure and central metals of TBPOMPc play a critical role in the sensitivity of NH_3, as evidenced from the scanning tunneling microscopy, current–voltage characteristics, and electrochemical impedance spectra.

Received 6th March 2017
Accepted 7th April 2017

DOI: 10.1039/c7ra02740k

rsc.li/rsc-advances

1. Introduction

NH_3 as a highly toxic gas is widely used in refrigeration, refining, manufacturing, cleaning, and nitrogenous fertilizers.[1,2] Exposure to high concentrations of NH_3 (*ca.* > 300 ppm) can cause serious health problems in humans.[3] To date, a number of studies have been reported on NH_3 sensors such as inorganic, inorganic oxide/dioxide, and conducting polymers.[4–7] However, most of these sensors cause high power consumption and exhibit low response to low concentration of NH_3, poor selectivity, and slow recovery time at room temperature. Therefore, an NH_3 sensor that causes lower power consumption and exhibits higher sensitivity, better selectivity, and fast recovery time at room temperature is urgent and significant for human demand.

Reduced graphene oxide (RGO) as a novel carbon material has a broad prospect in the field of gas sensors due to its high electrical conductivity, high chemical activity, and large specific surface area, which is beneficial for charge transfer and gas adsorption and desorption.[8–10] RGO gas sensors have shown higher sensitivity for the detection of polar gases such as NO_2, NO, NH_3, CO_2, H_2S, *etc.*[11–19] However, these sensors require improvement in terms of their selectivity, recovery time, and response to low concentration of gases. Therefore, functionalization of RGO is important to improve its sensitivity, selectivity, and speed up the recovery time at room temperature.

The surface of RGO retains partially polar functional groups such as –COOH, –OH, C=O, $–O^-$, *etc.* All of these endow RGO with good dispersibility in the solvent and make the functionalization of RGO easy.[20–24] Metallophthalocyanine (MPc) is a well-known organic semiconductor material that has been identified as a promising gas sensor due to its macrocyclic π–π conjugated system with an interesting structure, physical properties, and convenient chemical modification. When the central metal and the peripherally substituted groups are changed, MPc sensor exhibits high sensitivity, good selectivity, steady reproducibility, and fast response and recovery at room temperature in the detection of NO_2, NH_3, CO, H_2, *etc.*[25–33] However, the MPc molecules tend to aggregate during the film formation process, which is not conducive to the charge transfer and physical adsorption

[a]*Key Laboratory of Functional Inorganic Material Chemistry, Ministry of Education, School of Chemistry and Materials Science, Heilongjiang University, Harbin 150080, P. R. China. E-mail: wangbin@hlju.edu.cn*

[b]*Shanghai Institute of Optics and Fine Mechanics, Chinese Academy of Sciences, Shanghai 201800, P. R. China. E-mail: yqwu@siom.ac.cn*

† Electronic supplementary information (ESI) available. See DOI: 10.1039/c7ra02740k

between gas molecules and MPc.[34–36] Therefore, considering the advantages of RGO and MPc, a gas sensor containing both RGO and MPc combined *via* π–π non-covalent hybridization can be obtained. Our group has reported a type of NH_3 sensors obtained *via* the functionalizing of RGO with tetra-α-isopentyloxymetallophthalocyanine (TIPOMPc, M = Cu, Ni, and Pb). The RGO/TIPOMPc hybrids exhibited superior NH_3-sensing performance.[37] To date, to the best of our knowledge, there are few reports related to the influence of central metals and the substituted group of MPc on the NH_3-sensing property of RGO/MPc hybrids. Herein, we demonstrated a type of NH_3 sensors that contains RGO modified by MPc with a rigid substituent group (4-*tert*-butylphenoxyl) and different central metals. Compared to the flexible chain substituted TIPOMPc, our results indicated that TBPOMPc with a rigid substituted group more effectively prevented the intermolecular aggregation formation. Its influence on the NH_3-sensing behavior was due to the following two aspects: one is the specific surface area of RGO/MPc hybrids and the other is the charge transfer resistance of RGO/MPc hybrids. RGO/TBPOMPc hybrids have larger specific surface area but smaller charge transfer resistance than RGO/TIPOMPc hybrids. The former is conducive to the physical adsorption and diffusion of gas molecules, thus reducing the response and recovery time;[38] the latter is beneficial to the electron transfer from NH_3 to TBPOMPc and the decrease of hole carrier, resulting in the enhancement of sensitivity and selectivity to NH_3.[39]

2. Experimental

2.1 Preparation of the RGO/TBPOMPc hybrids (M = Cu, Ni, and Pb)

Preparation of GO and TBPOMPc (M = Cu, Ni, and Pb). We synthesized micrometer-sized GO flakes from graphite powder using a modified Hummers method.[40] TBPOMPc was synthesized by refluxing (*p*-*tert*-butylphenoxyl)phthalonitrile with DBU and anhydrous $CuCl_2$, $NiCl_2$, and $PbCl_2$ in anhydrous isopentanol, followed by column chromatography separation according to an established procedure.[41] For a detailed description, see GO and TBPOMPc synthesis section in the ESI.†

Preparation of RGO/TBPOMPc (M = Cu, Ni, and Pb). The schematic of the interaction process for the preparation of RGO/TBPOMPc hybrids is illustrated in Fig. S1B.† The prepared GO was sonicated in DMF, and the TBPOMPc DMF solution was added to the abovementioned solvent, followed by sonication in the dark for about 2.0 h and continuous stirring for 24 h. After this, the final product was purified through filtration and centrifugation. Finally, the hybrid was obtained and dried in vacuum for 24 h. The GO/TBPOMPc hybrid was added to a solution of NaOH (pH = 11) and ultrasonicated for 90 min. Hydrazine hydrate (N_2H_4) was added to the abovementioned solution and the mixed solution was heated at 90 °C for 2.0 h followed by centrifugation at 9000 rpm. Finally, the product was washed with DI water and ethyl alcohol and dried in a vacuum oven at 80 °C for 24 h. For comparison, RGO was also prepared *via* the similar procedures without TBPOMPc.

2.2 Structural characterization

RGO/TBPOMPc hybrids were characterized *via* Fourier transform infrared spectroscopy (FTIR, PE instruments, Spectrum One FTIR spectrometer), Raman spectroscopy (JobinYvon HR800 with excitation from the 450 nm laser source), ultraviolet-visible spectroscopy (UV-vis, Perkin-Elmer Lambda 900 spectrophotometer), thermogravimetric analysis (TGA, Perkin-Elmer TGA-7 system), and X-ray photoelectron spectroscopy (XPS, Kratos AXIS Ultra DLD system using monochromatic Al Kα X-ray source 1486.6 eV). The surface morphology and thickness of the films deposited on the silicon wafer were investigated *via* atomic force microscopy (AFM, Digital Instrument Nanoscope IIIa), transmission electron microscopy (TEM, JEM 2100 instrument at 200 kV), and scanning electron microscopy (SEM, Hitachi S4800). The film thicknesses of RGO/TBPOMPc placed on the electrodes were investigated *via* a stylus surface profilometer (KLA-Tencor, Alpha-step D-100 Stylus Profiler).

2.3 NH_3-sensing test

The sensing device was a 5 × 5 mm interdigitated electrode; it was fabricated using beam lithography on Al_2O_3 substrate through sputtering Au as a conductor layer, and the RGO/TBPOMPc hybrid was dispersed in DMF to create a suspension (0.5 mg mL^{-1}, 10 mL) by ultrasonication for 2 h. Then, a 2 μL suspension was spotted on the gold electrodes. After annealing treatment at 100 °C for 1 h in an Ar flow to remove the residual DMF, the RGO/TBPOMPc hybrid was connected with the gold fingers. Fig. S2† shows film thicknesses of RGO/TBPOMPc (M = Cu, Ni, and Pb) placed on the electrodes. The results show that the film thicknesses are about 80 nm. For comparison, a gas sensor of free RGO was also fabricated *via* similar procedures.

The sensor testing was carried out under practical conditions (*i.e.* room temperature 25 °C, relative humidity 50% RH; NH_3 and N_2 (99.9%) were purchased from GuangMing Research and Design Institute of Chemical Industry, PR China) using a homemade gas sensing measurement system.[37,51] One typical sensing test cycle has three steps in a sequential manner: first, N_2 (99.999% purity) was introduced into the sensing chamber (2 L min^{-1}) to obtain a baseline until the resistance remained unchanged for about 30 min. Second, different concentrations of NH_3, varying from 0.3 ppm to 3200 ppm, were injected into the chamber and the fan inside the chamber was turned on to make the gas uniform. We observed and obtained the resistance value when it remained unchanged for about 10 min. Finally, 99.999% purity N_2 (2 L min^{-1}) was introduced again for sensor recovery. Multiple testing cycles were performed by continuously repeating the same test several times. The room temperature dynamic sensing response sensitivity S was defined as $\Delta R/R = (R_g - R)/R$, where R is the average sensor resistance in the presence of N_2 and R_g is the sensor resistance after exposure to NH_3 gas. The response and recovery time were defined as the times needed to reach 90% of the final resistance.

2.4 The influence of MPc with a rigid substituted group on the NH_3-sensing behavior

The self-assembly behavior of TBPOMPc and TIPOMPc on the surface of RGO was investigated *via* scanning tunneling microscopy (STM, UNISOKU USM1400SA); the specific surface area of both RGO/TBPOMPc and RGO/TIPOMPc were investigated by N_2 adsorption and desorption analysis (Micromeritics TriStar II), and the samples were out gassed for 18 h at 90 °C under vacuum before carrying out the measurements. The pore size distribution was calculated using the Barrett–Joyner–Halenda (BJH) method. The current–voltage (*I–V*) characteristics of the fabricated sensors were measured using a Keithley 4200 semiconductor parameter analyzer with a two-point probe setup *via* sweeping the potential between −2 and +2 V under a 0.01 V s^{-1} scan rate. Electrochemical impedance spectra (EIS) were obtained using an IM6e electrochemical working station at room temperature (frequency range from 0.01 Hz to 100 kHz at the open circuit potential with a 5 mV amplitude).

3. Results and discussion

3.1 Structural characterization

The FTIR spectra of RGO before and after modification by TBPOMPc are shown in Fig. 1(A) and S3.† The typical peaks of RGO are located at 3427 cm^{-1} and 1059 cm^{-1}, which correspond to the O–H stretching and vibration mode of absorbed water. The peak around 1507 cm^{-1} corresponds to the ν(C–O–C) frequency. After modification, the characteristic peaks of TBPOMPc and RGO were found in the RGO/TBPOMPc hybrids (such as RGO/TBPOCuPc) at about 2955 cm^{-1}, 1507 cm^{-1}, 1252 cm^{-1}, 581 cm^{-1}, and 543 cm^{-1}. All these observations indicate that RGO/TBPOMPc hybrids were successfully obtained.

The UV-vis absorption spectra of TBPOMPc (2.0×10^{-3} mol L^{-1}, 25 °C), RGO, and RGO/TBPOMPc hybrids (0.1 mg mL^{-1}, 25 °C) in DMF solutions are given in Fig. 1(B) and S4.† TBPOMPcs show typical electronic absorption spectra with two strong absorption regions. The first region at about 335 nm (B-band) originates from the a_{2u} (HOMO) → a_{eg} (LUMO) transition, and the second region at about 600–700 nm (Q-band) is attributed to the transition from the a_{1u} (HOMO) to the a_{eg} (LUMO). For the typical electronic absorption region of RGO at about 255 nm, the weak absorbance is attributed to the poor dispersion in DMF. After RGO was modified with TBPOMPc, the characteristic peak of RGO red-shifted at about 300 nm, and the Q-band of TBPOMPc (M = Cu, Ni, and Pb) broadened with the decreasing intensity and red-shifted at about 26 nm, 53 nm, and 5 nm, respectively. All of them indicate the electron transfer from the electron donor TBPOMPc to the electron accepter RGO, which proves the strong π–π interaction between RGO and TBPOMPc.[42,43]

Fig. 2(A–C) shows the Raman spectra of RGO before and after modification by TBPOMPc. RGO shows a (G) peak at 1591 cm^{-1} and a (D) peak at 1367 cm^{-1}, which are the characteristic peaks of sp^2 and sp^3 hybridized carbon atoms in graphene that distinguish the order and disorder/defect in the structure, respectively.[44] After modification, the (G) peak and (D) peak appeared in RGO/TBPOMPc as well, which evidently indicated that RGO/TBPOMPc hybrids were obtained. The G band (~1591 cm^{-1}) corresponds to the first-order scattering of the E_{2g} mode observed for the sp^2 carbon domain, whereas the D band (~1367 cm^{-1}) is attributed to a common feature of the sp^3 defect in carbon. As a consequence, the intensity ratio I_D/I_G is usually a measure of the disorder/defect in graphene and further explains the covalent or non-covalent modification of graphene.[45] After modification, no obvious difference in the I_D/I_G of RGO/TBPOMPc (0.90) and the I_D/I_G of RGO (0.91) was observed, which evidently indicated that RGO/TBPOMPc hybrids were obtained *via* non-covalent hybridization. The (G) peak of RGO/TBPOMPc (M = Cu, Ni, and Pb) shifted to a short wavelength by about 4 cm^{-1}, 9 cm^{-1}, and 7 cm^{-1}, respectively; moreover, the intensity of pyrrole C=C stretching (about 1530 cm^{-1}), C–N stretching (about 1350 cm^{-1}), and isoindole ring stretching (about 1450 cm^{-1}) of TBPOMPc obviously decreased. All these observations indicate strong π–π electronic interaction between RGO and TBPOMPc. TBPOMPc provides abundant charge carrier to RGO and raises the Fermi level.[46–48]

The thermogravimetric analyses (TGA) results of RGO, TBPOMPc, and RGO/TBPOMPc hybrids are shown in Fig. 2(D). For the analyses, the samples were vacuum dried at 90 °C, the temperature was increased from 20 °C to 800 °C at 20 °C min^{-1}, and the flow rate of oxygen was 100 mL min^{-1}. The results show that the weight loss rate of RGO was about 2% when the temperature was below 600 °C, and it is probably due to water and solvent evaporation, which were adsorbed on the surface of RGO. When the temperature was increased to 600 °C, the weight

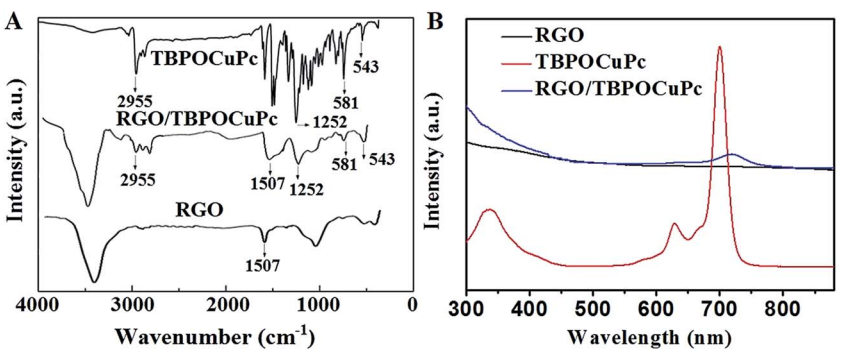

Fig. 1 (A) FTIR spectra and (B) UV-vis absorption spectra of RGO, RGO/TBPOCuPc, and TBPOCuPc.

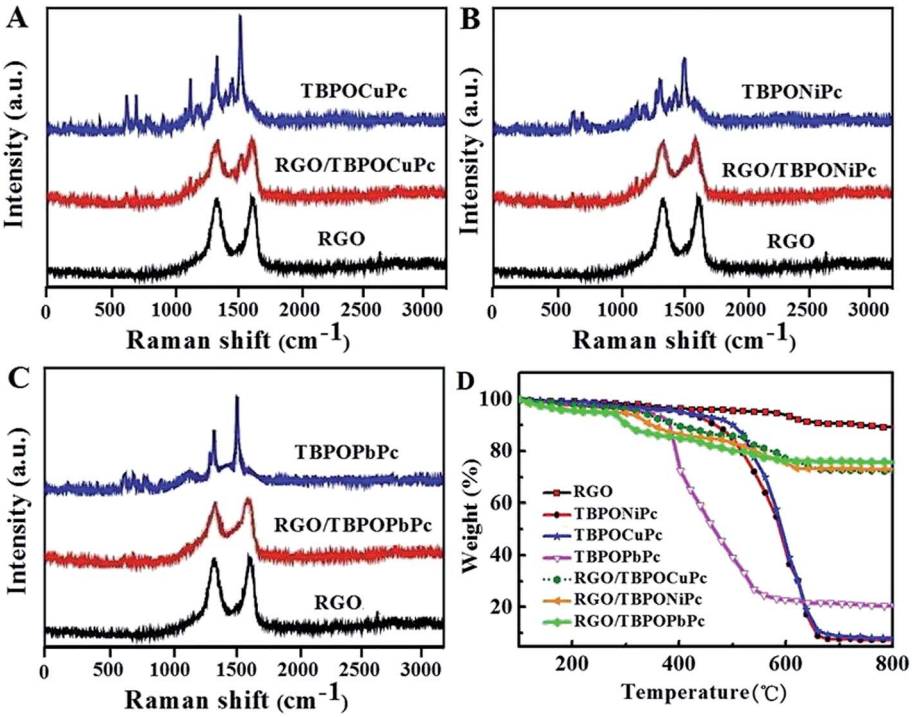

Fig. 2 (A–C) Raman spectra of RGO, TBPOMPc, and RGO/TBPOMPc hybrids, respectively, and (D) thermogravimetric analysis results of RGO, TBPOMPc, and RGO/TBPOMPc hybrids.

loss rate of RGO was about 10%, which was caused by the thermal decomposition of oxygen-containing groups on the sheet edge of RGO. The decomposition temperature of TBPOMPc was above 400 °C. When the temperature was increased above 650 °C, TBPOMPc completely decomposed, and the final decomposition product was MO. The weight loss rates are 91% (TBPOCuPc), 93% (TBPONiPc), and 80% (TBPOPbPc), which is consistent with the theoretical weight loss rate of TBPOCuPc (93.2%), TBPONiPc (93.6%), and TBPOPbPc (83.4%), respectively. The decomposition temperature of RGO/TBPOMPc hybrids is above 350 °C, ranging from 350 °C to 700 °C, and all the hybrids have a fast weight loss rate, which indicates that TBPOMPc were combined with RGO *via* π–π* non-conjugated.[49,50] Above 700 °C, the RGO/TBPOMPc hybrids completely decomposed, and the weight loss rate of RGO/TBPOCuPc, RGO/TBPONiPc, and RGO/TBPOPbPc was 27%, 28%, and 24%, respectively. Fig. S5† shows the thermogravimetric analysis results of RGO, TIPOMPc, and RGO/TIPOMPc hybrids. Similar to RGO/TBPOMPc, TG analyses implied that TIPOMPc content in the hybrids ranged from 16.9 to 17.8 wt%.

XPS was also employed to confirm the successful attachment of RGO/TBPOMPc hybrids and demonstrate charge transfer from TBPOMPc to RGO. As shown in Fig. 3(A), RGO/TBPOMPc hybrids exhibited the characteristic peaks of C 1s, N 1s, and O 1s and the characteristic peaks of Cu 2p (934.9 eV), Ni 2p (855.6 eV), and Pb 4f (138.6 eV). As shown in Fig. 4(E), the N 1s peaks of RGOTBPO/MPc hybrids consist of two split peaks, which are attributed to two groups of four nitrogen atoms in different chemical environments in the molecule and further suggests that the RGO/TBPOMPc hybrids were successfully prepared. Fig. 3(B–D) show that compared with the Cu 2p: 934.5 eV, Ni 2p: 855.5 eV, and Pb 4f: 137.8 eV peaks of TBPOMPc, the Cu 2p (934.8 eV), Ni 2p (855.6 eV), and Pb 4f (138.6 eV) peaks of RGO/TBPOMPc red-shifted by about 0.4 eV, 0.1 eV, and 0.8 eV, respectively; this also agrees with the charge transfer phenomena of the RGO/TBPOMPc hybrids and their N 1s XPS peak shifts to higher binding energy compared with that of TBPOMPc (as shown in Fig. 3(E)). These phenomena indicate charge transfer from TBPOMPc to RGO in the hybrids. The binding energy is correlated to the electron density around the nucleus (the lower the electronic density, the higher the binding energy).[44]

3.2 Morphology analysis of the RGO/TBPOMPc hybrids

The morphologies of RGO and RGO/TBPOMPc hybrids were investigated *via* AFM, SEM, and TEM. The AFM analysis result is shown in Fig. 4(I–L). The cross-section analysis indicates that the average thickness of the RGO film is around 5 nm (Fig. S6A†), and the theoretical thickness of the single-layer graphene is about 0.35 nm,[45] which implies that the film is composed of ten layers. The thickness of the RGO/TBPOMPc hybrids is about 6 nm (Fig. S6B–D†); therefore, the AFM height confirms the non-covalent attachment of the TBPOMPc molecule to the RGO basal plane through π–π interaction.

The SEM images of RGO and RGO/TBPOMPc hybrids are shown in Fig. 4(A–D). RGO exhibits the flake-like morphology with a slightly folded edge and flat surface, which is a typical characteristic of a nanosheet-like structure. After hybridization of RGO with TBPOMPc, TBPOMPc overlaid the surface of RGO,

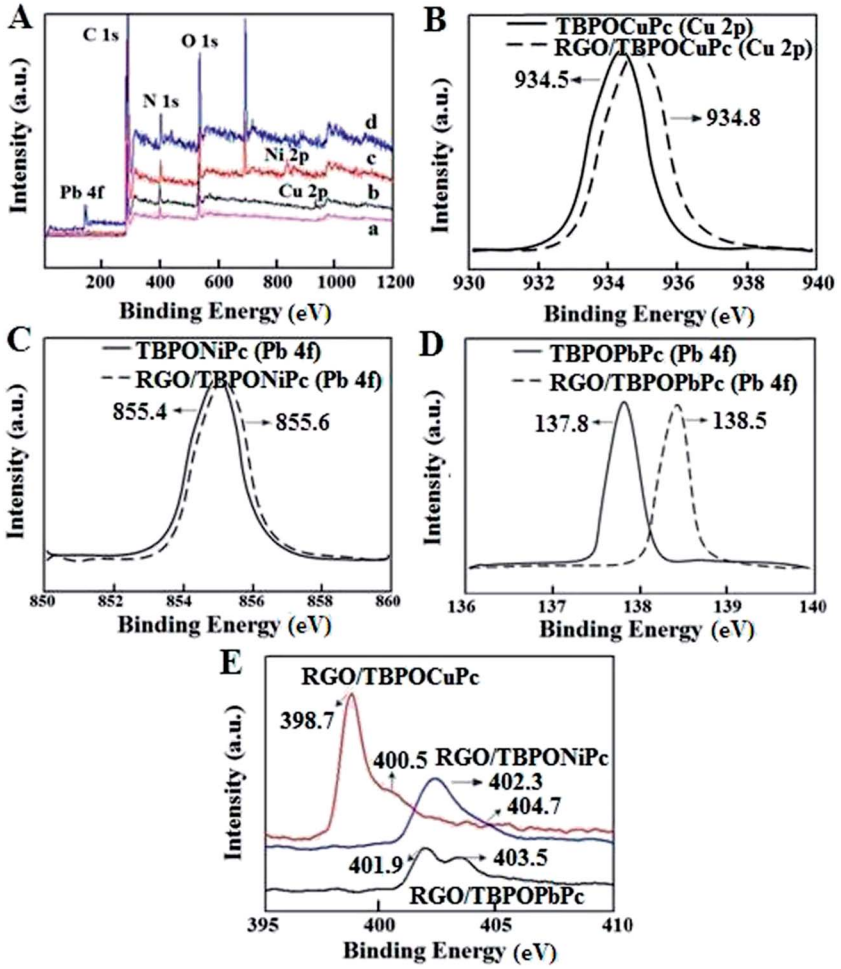

Fig. 3 (A) XPS analysis survey spectra of RGO (a), RGO/TBPOCuPc (b), RGO/TBPONiPc (c), and RGO/TBPOPbPc (d). (B) Cu 2p XPS spectra of TBPOCuPc and RGO/TBPOCuPc. (C) Ni 2p XPS spectra of TBPONiPc and RGO/TBPONiPc. (D) Pb 4f XPS spectra of TBPOPbPc and RGO/TBPOPbPc. (E) N 1s XPS spectra of RGO/TBPOMPc hybrids.

and the interface between the layers became fuzzy. The SEM images of RGO/TBPOMPc show that RGO/TBPOMPc has a porous surface morphology, which is helpful for the adsorption and desorption of gas molecules.

Fig. 4(E–H) show the TEM images and morphology analysis results of the RGO/TBPOMPc thin films. The TEM images indicate that RGO retained its lamellar structure and smooth surface; the layers overlapped each other, and the sheet thickness was about 5 nm. In contrast, RGO/TBPOMPc hybrids were obviously observed to have some cluster aggregates that contained TBPOMPc covered on the surface of RGO and formed a blurry rough layer. This further confirmed RGO/TBPOMPc formation *via* π–π non-covalent hybridization.

3.3 NH_3-sensing properties of the RGO/TBPOMPc hybrids

Fig. 5(A) and S7(A–C)† show the variations of the film resistance with time in the presence of NH_3 (0.3–3200 ppm) at room temperature. The results showed that the resistance of sensors dramatically increased with the increasing concentration of NH_3, and all the RGO/TBPOMPc sensors recovered to the original resistance value in the absence of NH_3. For pure RGO, it is hard to recover the resistance of the RGO sensor to the original resistance with the increasing concentration of NH_3. It indicates the improved recovery performance of the RGO/TBPOMPc hybrids. For 400 ppm NH_3, the response/recovery times are as follows: RGO/TBPOCuPc (639 s/578 s), RGO/TBPONiPc (807 s/755 s), and RGO/TBPOPbPc (540 s/422 s), which suggest that the response/recovery of these sensors is faster than that of RGO/TIPOCuPc (849 s/687 s), RGO/TIPONiPc (916 s/833 s), and RGO/TIPOPbPc (887 s/447 s) sensors.[37,51] It indicates that RGO/TBPOMPc hybrids are beneficial for the adsorption and diffusion of NH_3 molecules.

Fig. S7(D)† shows the response of RGO and RGO/TBPOMPc hybrids to NH_3 (0.3–3200 ppm) at room temperature. The inset plot implies the response to the low concentration of NH_3 (0.3–50 ppm). It indicates that RGO/TBPOMPc has better sensitivity (~2%) towards NH_3 (0.3 ppm), and excellent linear response in the range of 0.3–50 ppm and saturation response towards NH_3 above 2000 ppm. For the RGO/TBPOMPc hybrid, the sensitivity to NH_3 (400 ppm) was as follows: RGO/TBPOCuPc (12.2%), RGO/TBPONiPc (13.6%), and RGO/TBPOPbPc (18.6%), which is higher than those of RGO (7.2%), RGO/TIPOCuPc

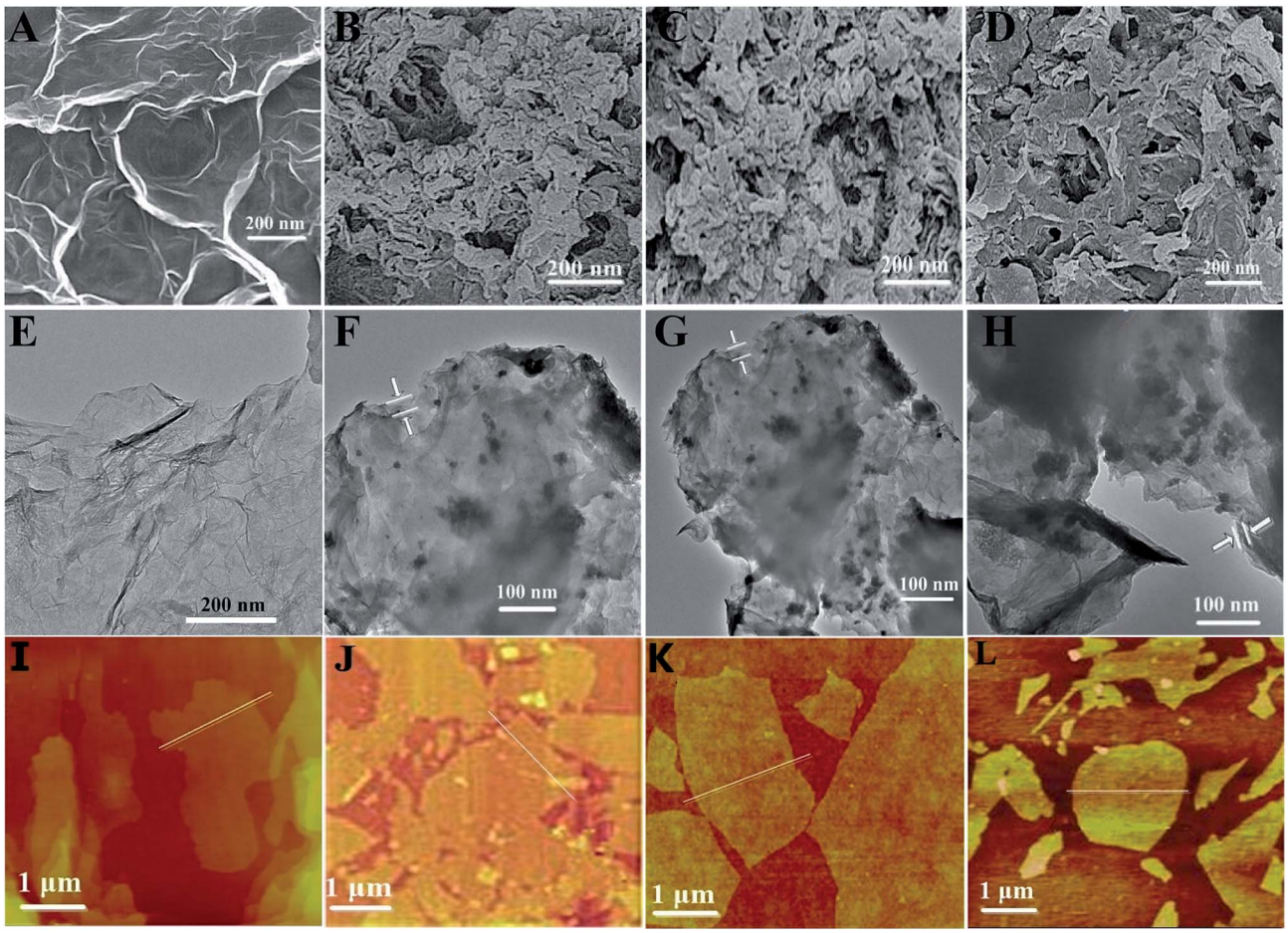

Fig. 4 (A–D) Typical SEM images of RGO (A), RGO/TBPOCuPc (B), RGO/TBPONiPc (C), and RGO/TBPOPbPc hybrids (D). (E–H) The TEM images of RGO (E), RGO/TBPOCuPc (F), RGO/TBPONiPc (G), and RGO/TBPOPbPc hybrids (H). (I–L) The AFM images of RGO (I), RGO/TBPOCuPc (J), RGO/TBPONiPc (K), and RGO/TBPOPbPc hybrids (L).

(11.5%), RGO/TIPONiPc (10.2%), and RGO/TIPOPbPc (11.4%). As the concentration of NH_3 was decreased to 0.3 ppm, the sensitivity to NH_3 (0.3 ppm) was as follows: RGO/TBPOCuPc (1.2%), RGO/TBPONiPc (1.6%), and RGO/TBPOPbPc (2.2%), which is still higher than that of RGO (0.3%), RGO/TIPOCuPc (1.8%), RGO/TIPONiPc (1.0%), and RGO/TIPOPbPc (1.4%).[51]

The RGO/TBPOMPc hybrids exhibit higher sensitivity than RGO/TIPOMPc hybrids towards the lower concentration of NH_3, especially the RGO/TBPOPbPc sensor that shows excellent gas sensing performance. Most of the MPc hybrids, such as CuPc and NiPc, present planar configuration; Pb^{2+} with a larger atom radius will be located on the plane of the Pc ring and form four pyramid structures due to the limitation of the central space of Pc.[32] The structure of the TBPOPbPc molecule is similar to those of PbPc[52] and PbNc[53] molecules, which are not planar. This molecular structure weakens the conjugating power of the phthalocyanine macrocycle, which is beneficial for the absorption of gases and central metal and makes it easier for the gas molecules to deeply adsorb;[54] thus, the RGO/TBPOPbPc sensor shows excellent gas sensing performance.

Reversibility is one of the most important characteristics for gas sensors. Fig. 5(B) shows the resistance of the RGO/TBPOPbPc hybrid exposed to 50 ppm NH_3 (five cycles). The results show that the films have good repeatability and no obvious degradation after consecutive measurements was observed. Moreover, under the atmospheric condition of 50% RH, the films were rather stable, and the resistance was almost unchanged within two weeks. After being exposed to air for about two months, the change in the resistance was within 2%. The response to NH_3 changed to only about 5%.

Selectivity is also an important property of gas sensors. We measured the sensing response of the RGO/TBPOPbPc sensor to several other gases including reducing gases, such as H_2 and CO, and an oxidizing gas such as NO_2. The sensing test cycle is the same as that for NH_3. Our results show that the RGO/TBPOPbPc sensor has an excellent selectivity for 25 ppm NH_3 among all the test gases. As shown in Fig. 5(C), the sensor has negligible response to both H_2 and CO (100 ppm). The result indicates that NH_3 is preferable for the RGO/TBPOMPc sensor among common reducing gases, which acted as an electron donor. NO_2 is an oxidization gas and an electron acceptor. The resistance of RGO/TBPOPbPc to 300 ppm NO_2 decreased, suggesting charge transfer from TBPOPbPc to the NO_2 molecule.

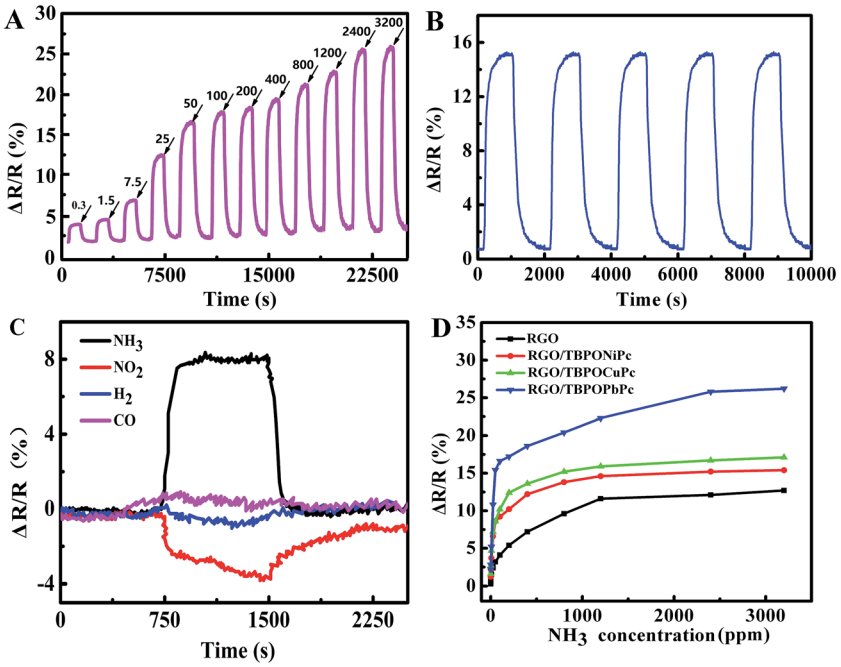

Fig. 5 (A) Response of RGO/TBPOPbPc sensors upon exposure to varying concentrations of NH_3; (B) five sensing cycles of the RGO/TBPOPbPc sensor exposed to 50 ppm NH_3; (C) cross-sensitivities to various gases for the RGO/TBPOPbPc sensor; (D) relationship of the response of RGO and RGO/TBPOMPc sensors to varying concentrations of NH_3.

3.4 The influence of rigid phenoxyl substituted MPc on NH_3-sensing property

Both RGO and MPc are p-type semiconductor materials, and the carriers are holes. NH_3 as an electron donor tends to increase the electron density of RGO or MPc; thus, the number of hole carriers is reduced, and the resistance of RGO or MPc is increased.[15,55] The gas sensing mechanism is mainly influenced by a physical process and a chemical process. The physical process includes the physical adsorption of gas molecules on the surface of a gas sensor and also the gas diffusion inside the sensing material, which affects the response and recovery times. The chemical process includes the charge transfer between gas and the sensing material, and the production of

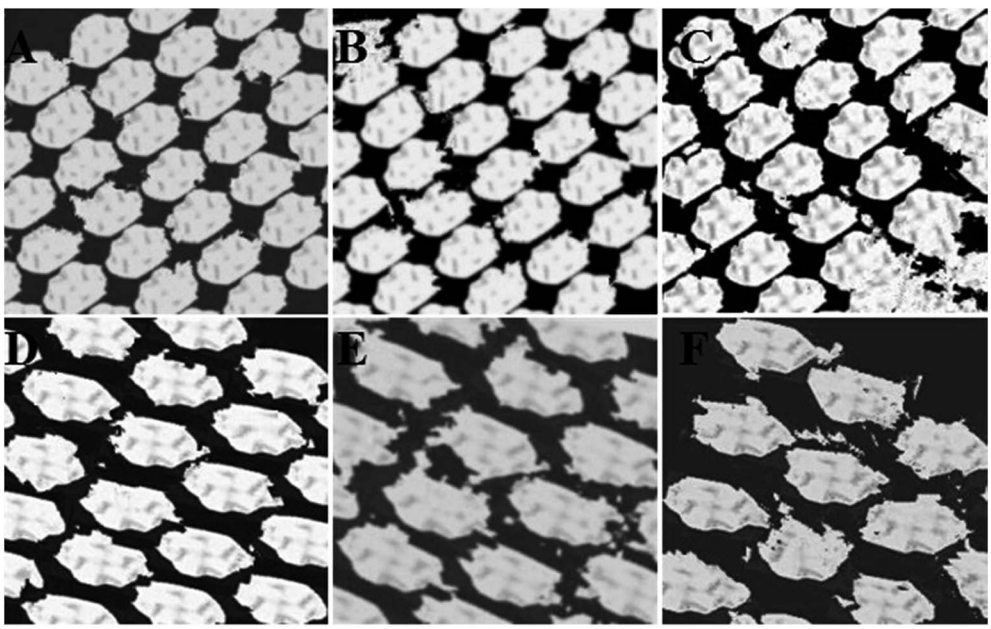

Fig. 6 High resolution STM images of RGO/TIPOCuPc (A), RGO/TIPONiPc (B), RGO/TIPOPbPc (C), RGO/TBPOCuPc (D), RGO/TBPONiPc (E), and RGO/TBPOPbPc (F), 10 nm × 10 nm; tunnel current: 200 pA; sample bias: 1.8 V.

a carrier, which affects the sensitivity and selectivity.[56,57] Therefore, the influence of phenoxyl substituted MPc on NH_3 sensing property was discussed based on this theory.

3.4.1 The self-assembly morphology analysis of TBPOMPc and TIPOMPc. The self-assembly behaviors of both TBPOMPc and TIPOMPc on the surface of RGO were investigated by scanning tunneling microscopy (STM). All the samples were dissolved in DMF (chromatographic purity) with a 2 μL sample solution dropped on the surface of RGO, then the STM tip was immersed in the solution, and scan imaging was carried out at room temperature. The tip material was Pt/Ir = 90/10, and the images were obtained in the constant current mode, with flattening to process the substrate tilt and scanning line illusion and low-pass was used to eliminate the noise in the scan. The results are shown in Fig. 6 and S8.† Large-scale STM images (Fig. S8†) show that the surface of RGO orderly arrayed and formed a wide range of grid structures. Each spot in the grid structure corresponds to a MPc molecule, and it indicates that the substrate lattice structure of RGO generated a template effect on the self-assembly process of MPc. From the high resolution STM images (Fig. 6), it was observed that all the MPc molecules exhibited a four-leaf-like structure. We found that each TIPOMPc molecule associates with four adjacent TIPOMPc molecules, and each grid cavity size is 1.37 nm^2 (TIPOCuPc), 1.42 nm^2 (TIPONiPc), and 1.22 nm^2 (TIPOPbPc). Under the same test conditions, each TBPOMPc molecule associated with two adjacent TBPOMPc molecules to form a linear structure, and the spacing of the straight chain was bigger than that of TIPOMPc; each grid cavity size was 2.44 nm^2 (TBPOCuPc), 2.32 nm^2 (TBPONiPc), and 2.53 nm^2 (TBPOPbPc). The bigger grid cavity of TBPOMPc is beneficial for the permeability and desorption of gas molecules. The discrepant self-assembly structure is mainly attributed to different substituted groups on the MPc ring, and the proposed self-assembly molecular structure model of MPc is shown in Fig. S9.† 4-*tert*-Butylphenoxyl has a rigid structure and larger steric hindrance, and it effectively prevented the aggregation of TBPOMPc molecules. However, isopentyloxyl has a flexible structure and smaller steric hindrance; thus, it is easy for these molecules to intertwine with each other.

The different surface area A_s of RGO and RGO/MPc were determined by N_2 adsorption and desorption isotherms. The A_s was calculated by Brunauer–Emmett–Teller (BET) at the relative pressure of 0.05–0.30, and the pore size distribution was calculated using the Barrett–Joyner–Halenda (BJH) method for isotherm desorption branch, and the results are shown in Fig. S10.† It indicates that all the adsorption isotherms are typical IV type with an H_4 hysteresis loop, which are characteristic of a mesoporous structure. The curve slowly increased at the low P/P_0 region (0.0–0.1) due to a small amount of microporous adsorbent, and as the pressure increased (0.3–0.8), the isotherm slope increased, exhibited a mesoporous adsorbent; at the high P/P_0 region (0.9–1.0), the isotherm slope that was still increasing exhibited macroporous adsorption, which is consistent with the SEM images. As N_2 condensation took place in the mesoporous channels, the desorption–adsorption isotherm is not coincidental, showing a typical H_4 hysteresis loop, which is characteristic of a typical layered mesoporous structure. At the P/P_0 of 0.5–0.8, adsorption capacity rapidly increased; the P/P_0 location reflects pore sizes, and the changing range of P/P_0 can be used as a measure of the mesoporous uniformity. Under the condition of the same central metal, the specific surface areas of RGO/TBPOMPc films are bigger than those of RGO/TIPOMPc films because the rigid substituted TBPOMPc effectively prevented the aggregate formation and increased the molecular spacing, whereas a flexible chain substituted TIPOMPc has a tendency to locate adjacent to each other for less steric hindrance. Large specific surface area is favorable for the adsorption and desorption of gas molecules. From the inset images shown in Fig. S10,† it was observed that the mesopores of RGO/TBPOMPc are mainly distributed in the vicinity of 5–30 nm, the average pore diameter is about 12.1 nm, and mesoporous distribution is centered at about 12 nm. Comparison of the pore volume of both RGO/TBPOMPc and RGO/TIPOMPc in the 2.5–5.0 nm range at the same P/P_0 indicates that RGO/TBPOMPc has a bigger pore volume. TIPOMPc molecules are closely adjacent to each other and overlap with each other; thus, it has a higher capacity to shadow and block the micropores, thus making the pore volume smaller. Hence, RGO/TBPOMPc hybrids show better sensing performance towards NH_3 than the RGO/TIPOMPc hybrids (Fig. 5(D)) (Table 1).

3.4.2 *I–V* and EIS analysis. To explore the effect of the substituent groups, the *I–V* characteristics of the RGO/TBPOMPc and RGO/TIPOMPc sensors with the same mass loading on IDEs were investigated (Fig. 7(A) and S11†). The linearity and symmetry of the *I–V* curves suggest an ohmic contact between the samples and gold electrodes. Evidently, the device current of various hybrids at the same voltage decreases in the order of RGO > RGO/TBPOMPc > RGO/TIPOMPc. Low current means the sensor has a relatively high resistance. For RGO/TBPOMPc and RGO/TIPOMPc hybrids, the decrease in device current is possibly caused by the intrinsically high resistance of TBPOMPc and TIPOMPc, with the donation of electrons from the p-type TBPOMPc and TIPOMPc to the p-type RGO backbone.[58] Since they have the same central metals, the distinct difference in the device current of the RGO/TBPOMPc

Table 1 The A_s ($m^2\ g^{-1}$) and V_m ($cm^3\ g^{-1}$) of RGO and RGO/MPc

Sample	RGO	RGO/TBPOCuPc	RGO/TIPOCuPc
A_s ($m^2\ g^{-1}$)	447.9	205.4	151.2
V_m ($cm^3\ g^{-1}$)	0.57	0.33	0.31
Sample	RGO	RGO/TBPONiPc	RGO/TIPONiPc
A_s ($m^2\ g^{-1}$)	447.9	197.0	171.4
V_m ($cm^3\ g^{-1}$)	0.57	0.33	0.29
Sample	RGO	RGO/TBPOPbPc	RGO/TIPOPbPc
A_s ($m^2\ g^{-1}$)	447.9	277.1	190.1
V_m ($cm^3\ g^{-1}$)	0.57	0.41	0.32

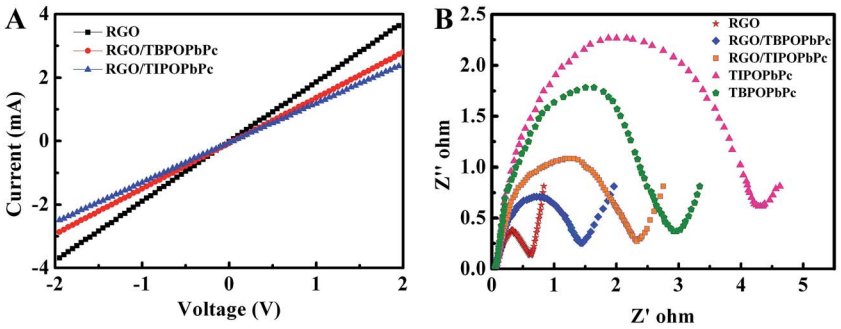

Fig. 7 *I–V* curves of RGO and RGO/TBPOPbPc and RGO/TIPOPbPc hybrids (A) and EIS measurements of RGO, RGO/TIPOPbPc, RGO/TBPOPbPc, TIPOPbPc, and TBPOPbPc electrodes in a 6 M KOH aqueous solution (B).

and RGO/TIPOMPc hybrids was ascribed to the substituent groups. Alkoxy (–OR) groups have stronger electron-donating capability than phenoxy (–OPh) groups. Relative to RGO/TBPOMPc, the RGO/TIPOMPc-containing alkoxy groups can provide more electrons to combine with the holes in p-type semiconductors of TIPOMPc and RGO.[59] The combination of electrons and holes can reduce the carrier concentration of the system, leading to further increase in the resistances of RGO/TIPOMPc hybrids. Hence, their responses towards NH_3 are not as good as that of the RGO/TBPOMPc hybrid (Fig. 5(D)).

Electrochemical impedance spectroscopy (EIS) is a principal method to examine the fundamental behavior, such as charge transfer impedance (R_{ct}), solution impedance (R_s), *etc.*, of modified electrode materials. The impedances for MPc, RGO, and RGO/MPc were tested in the frequency range from 0.01 Hz to 100 kHz at the open circuit potential with 5 mV amplitude. The results are shown in Fig. 7(B) and S12.† The radius of the semicircle impedance loop in the high frequency region could reflect the resistance to mass transfer/diffusion rate of ions from the electrode to the modified material. The equivalent circuit model exhibits that the entire capacitor circuit is constituted by R_s, Z_w, R_{ct}, C, and Q, as shown in Fig. S12C.† R_s is the sum of the contact resistance and material resistance, which is related to the ionic conductivity of the electrolyte and electronic conductivity of the electrodes and current collectors. Z_w is the Warburg resistance (45° inclined curve) related to the ion diffusion/transport in the electrolyte. R_{ct} is the resistance for blocking the ions from entering the pores of the electrode materials and also for blocking the movement of the ions into the solution and separator. C and Q present the capacitor layers, which are formed during the charge–discharge process. The values of impedance calculated using ZSimpWin software are summarized in Table 2. Obviously, the R_{ct} value reflects the conductivity that has a great influence on the charge transfer from NH_3 to gas sensitive material. As we expected, the R_{ct} value of the RGO/TBPOMPc hybrid is higher than that of RGO but lower than that of TBPOMPc, and for the RGO/TIPOMPc hybrid, it is the same as that for the RGO/TBPOMPc hybrid. On the one hand, RGO has poor selectivity and low sensitivity towards the low concentration of NH_3 due to its excellent conductivity. Too fast charge mobility could lead to weak electronic interaction effect between RGO and NH_3 or similar reducing gas (low concentration); thus, the response value is hard to detect. The R_{ct} value of the RGO/MPc hybrids shows a marked increase than that of RGO, which indicates that an electron is first transferred from NH_3 to MPc and then it enhances the electronic interaction effect between NH_3 and RGO. Therefore, the selectivity and sensitivity of the RGO/MPc sensor will be enhanced over those of the RGO sensor. On the other hand, RGO/MPc hybrids effectively improve the conductivity of MPc, which favors the electron transfer from NH_3 to MPc, thus changing the electron density of MPc and the number of hole carriers. Therefore, the sensitivity of RGO/MPc to NH_3 is higher than that of MPc. Under the conditions of the same central metal, the R_{ct} value follows the order TBPOMPc < TIPOMPc and RGO/TBPOMPc < RGO/TIPOMPc. The reason for this is the rigid phenoxyl

Table 2 The values of R_{ct} calculated through the impedance spectra using ZSimpWin software

Sample	RGO	TBPOCuPc	TIPOCuPc	RGO/TBPOCuPc	RGO/TIPOCuPc
R_{ct} (Ω)	0.565	2.662	3.736	1.355	1.901
Sample	RGO	TBPONiPc	TIPONiPc	RGO/TBPONiPc	RGO/TIPONiPc
R_{ct} (Ω)	0.565	3.176	4.226	1.654	2.134
Sample	RGO	TBPOPbPc	TIPOPbPc	RGO/TBPOPbPc	RGO/TIPOPbPc
R_{ct} (Ω)	0.565	2.560	4.154	1.332	2.219

substituent of TBPOMPc that effectively prevents the aggregation formation of MPc; thus, the intermolecular electron cloud does not effectively overlap and the electronic interaction effect of TBPOMPc is lower than that of TIPOMPc. The lower the values of R_{ct}, the stronger the electron transport. As a result, the resistance of charge transfer from NH_3 to TBPOMPc is reduced, and the conductivity of TBPOMPc is enhanced. Therefore, the NH_3 sensitivity of RGO/TBPOMPc is higher than that of RGO/TIPOMPc.

4. Conclusions

In summary, we demonstrated the fabrication and application of RGO/TBPOMPc (M = Cu, Ni, and Pb) in NH_3 gas sensors at room temperature. RGO/TBPOMPc hybrids with rigid phenoxyl substituted groups were synthesized by noncovalent assembly. Compared to RGO/TIPOMPc sensors, the obtained RGO/TBPOMPc sensors, especially the RGO/TBPOPbPc sensor, show high sensitivity (15.5% to 50 ppm NH_3 with a LOD of 300 ppb), excellent stability and reproducibility, fast response/recovery, and excellent selectivity. The significant enhancement in NH_3 sensing is associated with the combination of TBPOMPc with a rigid phenoxyl substituted group and RGO. First, the rigid phenoxyl substituted MPc prevents the aggregation behavior of TBPOMPc molecules on the surface of RGO. As a result, RGO/TBPOMPc hybrids have larger specific area and lower charge transfer resistance, which is propitious for the adsorption and diffusion of gas molecules and charge transfer from NH_3 to TBPOMPc. Second, as a conductive agent, RGO provides continuous pathways for charge transportation, leading to a fast and sensitive response. More importantly, charge transfer between TBPOMPc and RGO can be achieved *via* π–π stacking interaction. In this system, the rigid structure and central metals of TBPOMPc have a great influence on the NH_3-sensing performance. It is suggested that through changing the peripherally substituted group and central metals of MPc, we could regulate its molecular aggregation behavior on the surface of RGO to adjust the NH_3-sensing behavior.

Acknowledgements

We gratefully acknowledge the financial support received from the National Natural Science Foundation of China (51202061 and 51002046), the Natural Science Foundation for the Returned Overseas Scholars of Heilongjiang Province (LC2012C02), the Natural Science of Heilongjiang Province (B201308), the Postdoctoral Science-Research Developmental Foundation of Heilongjiang Province (LBH-Q11015) and the Innovative Talents Program for the Returned Overseas Scholars of Harbin (2012RFLXG031), and the Opening Project Foundation of Key Laboratory of Functional Inorganic Material Chemistry (Heilongjiang University), Ministry of Education.

References

1 S. M. Cui, H. H. Pu, G. H. Lu, Z. H. Wen, E. C. Mattson, C. J. Hirschmugl, M. Gajdardziska-Josifovska, M. Weinert and J. H. Chen, *ACS Appl. Mater. Interfaces*, 2012, **4**, 4898.
2 X. L. Huang, N. T. Hu, R. G. Gao, Y. Yu, Y. Y. Wang, Z. Yang, E. Siu-Wai Kong, H. Wei and Y. F. Zhang, *J. Mater. Chem.*, 2012, **22**, 22488.
3 K. P. Yoo, K. H. Kwon, N. K. Min, M. J. Lee and C. J. Lee, *Sens. Actuators, B*, 2009, **143**, 333.
4 D. J. Late, Y. K. Huang, B. Liu, J. Acharya, S. N. Shirodkar, J. J. Luo, *et al.*, *ACS Nano*, 2013, **7**, 4879.
5 S. Chen and G. Sun, *ACS Appl. Mater. Interfaces*, 2013, **5**, 6473.
6 P. K. Kannan and R. Saraswathi, *J. Mater. Chem. A*, 2014, **2**, 394.
7 O. S. Kwon, S. J. Park, H. Yoon and J. Jang, *Chem. Commun.*, 2012, **48**, 10526.
8 S. Mao, G. H. Lu and J. H. Chen, *J. Mater. Chem. A*, 2014, **2**, 5573.
9 W. J. Yuan and G. Q. Shi, *J. Mater. Chem. A*, 2013, **1**, 10078.
10 T. Wang, D. Huang, Z. Yang, S. S. Xu, G. L. He, X. L. Li, N. T. Hu, G. L. Yin, D. N. He and L. Y. Zhang, *Nano-Micro Lett.*, 2016, **8**, 95.
11 N. Hu, Z. Yang, Y. Wang, L. Zhang, Y. Wang, X. Huang, H. Wei, L. Wei and Y. Zhang, *Nanotechnology*, 2014, **25**, 025502.
12 Y. Wang, L. Zhang, N. Hu, Y. Wang, Y. Zhang, Z. Zhou, Y. Liu, S. Shen and C. Peng, *Nanoscale Res. Lett.*, 2014, **9**, 251.
13 Y. P. Dan, Y. Lu, N. J. Kybert, Z. T. Luo and A. T. C. Johnson, *Nano Lett.*, 2009, **9**, 1472.
14 P. A. Pandey, N. R. Wilson and J. A. Covington, *Sens. Actuators, B*, 2013, **183**, 478.
15 S. S. Varghese, S. Lonkar, K. K. Singh, S. Swaminathan and A. Abdala, *Sens. Actuators, B*, 2015, **218**, 160.
16 E. Llobet, *Sens. Actuators, B*, 2013, **179**, 32.
17 H. Meng, W. Yang, K. Ding, L. Feng and Y. F. Guan, *J. Mater. Chem. A*, 2015, **3**, 1174.
18 S. M. Hafiz, R. Ritikos, T. J. Whitcher, N. M. Razib, D. C. S. Bien, *et al.*, *Sens. Actuators, B*, 2014, **193**, 692.
19 S.-J. Choi, B.-H. Jang, S.-J. Lee, B. K. Min, A. Rothschild and I.-D. Kim, *ACS Appl. Mater. Interfaces*, 2014, **6**, 2588.
20 H. J. Salavagione, A. M. Díez-Pascual, E. Lázaro, S. Verab and M. A. Gómez-Fatoua, *J. Mater. Chem. A*, 2014, **2**, 14289.
21 Z. B. Ye, Y. D. Jiang, H. L. Tai and Z. Yuan, *Integr. Ferroelectr.*, 2014, **154**, 73.
22 S. Yoo, X. Li, Y. Wu, W. H. Liu, X. L. Wang and W. H. Yi, *J. Nanomater.*, 2014, **2014**(7), 1.
23 P. G. Su and H. C. Shieh, *Sens. Actuators, B*, 2014, **190**, 865.
24 L. Zhou, F. Shen, X. Tian, D. Wang, T. Zhang and W. Chen, *Nanoscale*, 2013, **5**, 1564.
25 F. I. Bohrer, C. N. Colesniuc, J. Park, M. E. Ruidiaz, I. K. Schuller, A. C. Kummel and W. C. Trogler, *J. Am. Chem. Soc.*, 2009, **131**, 478.
26 B. Wang, X. Q. Zhou, Y. Q. Wu, Z. M. Chen, C. Y. He and X. Zuo, *Sens. Actuators, B*, 2012, **161**, 498.
27 T. Sizun, M. Bouvetn and J. Suisse, *Talanta*, 2012, **97**, 318.
28 X. J. Wang, S. L. Ji, H. B. Wang and D. H. Yan, *Sens. Actuators, B*, 2011, **160**, 115.
29 A. Singh, S. Samanta, A. Kumar, A. K. Debnath, R. Prasad, P. Veerender, V. Balouria, D. K. Aswal and S. K. Gupta, *Org. Electron.*, 2012, **13**, 2600.

30 S. Pochekailov, J. Nožár, S. Nešpůrek, J. Rakušan and M. Karásková, *Sens. Actuators, B*, 2012, **169**, 1.
31 T. Sizun, T. Patois, M. Bouvet and B. Lakard, *J. Mater. Chem.*, 2012, **22**, 25246.
32 G. Guillaud, J. Simon and J. P. Germain, *Coord. Chem. Rev.*, 1998, **178–180**, 1433.
33 B. Wang, Y. Q. Wu, X. L. Wang, Z. M. Chen and C. Y. He, *Sens. Actuators, B*, 2014, **190**, 157.
34 X. H. Liang, Z. M. Chen, H. Wu, L. X. Guo, C. Y. He, B. Wang and Y. Q. Wu, *Carbon*, 2014, **80**, 268.
35 Y. Y. Wang, N. T. Hu, Z. H. Zhou, D. Xu, Z. Wang, Z. Yang, H. Wei, E. S. W. Kong and Y. F. Zhang, *J. Mater. Chem.*, 2011, **21**, 3779.
36 J. H. Park, J. E. Royer, E. Chagarov, T. Kaufman-Osborn, M. Edmonds, T. Kent, *et al.*, *J. Am. Chem. Soc.*, 2013, **135**, 14600.
37 X. Q. Zhou, X. L. Wang, B. Wang, Z. M. Chen, C. Y. He and Y. Q. Wu, *Sens. Actuators, B*, 2014, **193**, 340.
38 F. Schedin, A. K. Geim, S. V. Morozov, *et al.*, *Nat. Mater.*, 2007, **6**, 652.
39 P. Li, Y. Ding, A. Wang, L. Zhou, S. H. Wei, Y. M. Zhou, *et al.*, *ACS Appl. Mater. Interfaces*, 2013, **5**, 2255.
40 S. Park, J. An, R. D. Piner, I. Jung, D. Yang, A. Velamakanni, S. T. Nguyen and R. S. Ruoff, *Chem. Mater.*, 2008, **20**, 6592.
41 K. Moriya, H. Enomoto and Y. Nakamura, *Sens. Actuators, B*, 1993, **13–14**, 412.
42 H. Z. Zhao, Y. Zhang, B. Zhao, Y. Y. Chang and Z. S. Li, *Environ. Sci. Technol.*, 2012, **46**, 5198.
43 X. Ling, J. X. Wu, W. G. Xu and J. Zhang, *Small*, 2012, **8**(9), 1365.
44 A. Chunder, T. Pal, S. I. Khondaker and L. Zhai, *J. Phys. Chem. C*, 2010, **114**, 15129.
45 M. J. Allen, V. C. Tung and R. B. Kaner, *Chem. Rev.*, 2010, **110**, 132.
46 H. J. Shin, S. M. Kim, S. M. Yoon, A. Benayad, K. K. Kim, S. J. Kim, H. K. Park, J. Y. Choi and Y. H. Lee, *J. Am. Chem. Soc.*, 2008, **130**, 2062.
47 V. Z. Poenitzsch, D. C. Winters, H. Xie, G. R. Dieckmann, A. B. Dalton and I. H. Musselman, *J. Am. Chem. Soc.*, 2007, **129**, 14724.
48 A. Das, S. Pisana, B. Chakraborty, S. Piscanec, S. K. Saha, U. V. Waghmare, K. S. Novoselov, H. R. Krishnamurthy, A. K. Geim, A. C. Ferrari and A. K. Sood, *Nat. Nanotechnol.*, 2008, **3**, 210.
49 N. Karousis, J. Ortiz, K. Ohkubo, T. Hasobe, S. Fukuzumi, A. Sastre-Santos and N. Tagmatarchis, *J. Phys. Chem. C*, 2012, **116**, 20564.
50 A. Ndiaye, P. Bonnet, A. Pauly, M. Dubois, J. Brunet, C. Varenne, K. Guerin and B. Lauron, *J. Phys. Chem. C*, 2013, **117**, 20217.
51 X. C. Li, B. Wang, X. L. Wang, X. Q. Zhou, Z. M. Chen, C. Y. He, Z. Y. Yu and Y. Q. Wu, *Nanoscale Res. Lett.*, 2015, **10**, 373.
52 Y. Iyechika, K. Yakushi, I. Ikemoto and H. Kuroda, *Acta Crystallogr., Sect. B: Struct. Crystallogr. Cryst. Chem.*, 1982, **38**, 766–770.
53 R. E. C. Clavijo, M. M. Campos-Vallette, M. S. Saavedra, A. Alvarado and G. E. Diaz, *Vib. Spectrosc.*, 1997, **14**, 79–85.
54 J. D. Wright, *Prog. Surf. Sci.*, 1981, **31**, 1–60.
55 C. W. Bauschlicher Jr and A. Ricca, *Phys. Rev. B: Condens. Matter Mater. Phys.*, 2004, **70**, 115409.
56 H. Chang, D. J. Lee, S. M. Lee and Y. H. Lee, *Appl. Phys. Lett.*, 2001, **79**, 3863.
57 J. J. Zhao, A. Buldum, J. Han and J. P. Lu, *Nanotechnology*, 2002, **13**, 195.
58 D. R. Kauffman, O. Kuzmych and A. Star, *J. Phys. Chem. C*, 2007, **111**, 3539.
59 H. Wu, Z. M. Chen, J. L. Zhang, F. Wu, C. Y. He, B. Wang, Y. Q. Wu and Z. Y. Ren, *J. Mater. Chem. A*, 2016, **4**, 1096.